Journal of Integrative Neuroscience

J. Integr. Neurosci. **2026**; 25(8): 52601
https://doi.org/10.31083/JIN52601

Original Research

Evaluating a Transparent Cranial Window for *In Vivo* Observation of μECoG Arrays on the Macaque Visual Cortex

Xinwei Wang[1,2,3], Xiangsheng Zeng[1,2,3], Chengpeng Li[1,2,3], Danling Hu[1,2,3], Hisashi Tanigawa[1,2,3,4,*]

[1]School of Brain Science and Brain Medicine, Zhejiang University School of Medicine, 310058 Hangzhou, Zhejiang, China
[2]National Key Laboratory of Brain and Computer Intelligence, Zhejiang University, 310058 Hangzhou, Zhejiang, China
[3]Key Laboratory for Biomedical Engineering of Ministry of Education, College of Biomedical Engineering and Instrument Science, Zhejiang University, 310027 Hangzhou, Zhejiang, China
[4]MOE Frontier Science Center for Brain Science and Brain-Machine Integration, School of Brain Science and Brain Medicine, Zhejiang University, 310012 Hangzhou, Zhejiang, China
*Correspondence: hisashi.q@gmail.com (Hisashi Tanigawa)
Academic Editor: Imran Khan Niazi
Submitted: 4 April 2026 Revised: 31 May 2026 Accepted: 3 June 2026 Published: 26 August 2026

Abstract

Background: High-density micro-electrocorticography (μECoG) provides the spatiotemporal resolution necessary to probe columnar-level cortical architecture. However, chronic multimodal interfacing is fundamentally challenged by aggressive post-surgical tissue responses that rapidly obscure optical access, in addition to localization uncertainties due to brain shift. In this study, established a transparent cranial window interface on the macaque visual cortex. To evaluate the feasibility of this approach, we primarily focused on assessing strategies to mitigate dural tissue regrowth and documenting the inherent biological complications (e.g., hemorrhage), while exploring the potential for direct, *in vivo* visual localization of μECoG arrays. **Methods:** A custom transparent chamber assembly integrated with a 64-channel μECoG array was implanted in the visual cortex of two rhesus macaques ($n = 2$). We compared two dural interface designs—a floating Tecoflex sheet versus a bonded silicone ring—to optimize optical clarity and interface stability. Physical stability of the electrodes relative to vascular landmarks was quantified. Electrophysiological performance was longitudinally evaluated using impedance monitoring, visual evoked potentials, and support vector machine (SVM) neural decoding to discriminate between red-green and black-white grating stimuli, with statistical significance assessed via bootstrap tests. **Results:** Regarding the biological and electrical interfaces, while long-term optical maintenance proved challenging due to tissue regrowth or hemorrhage, the bonded silicone ring design effectively mitigated peripheral tissue invasion. Electrophysiologically, array performance captured the dynamic biological transitions of the interface. Stable impedance profiles and statistically significant gamma-band (30–80 Hz) responses—modulating from initial widespread coverage (up to 100%) to restricted subsets (e.g., 16% at five months)—alongside robust SVM classification accuracy ($p < 0.001$) were tracked longitudinally. Additionally, as a preliminary observation in a single subject, the transparent window permitted the precise identification of electrode positions relative to cortical vasculature, revealing minor physical displacements (median = 0.20 mm) within the initial two weeks post-implantation. **Conclusions:** Comparing two dural interface designs highlights the mechanical and biological trade-offs required for chronic optical access, emphasizing that optimizing the mechanical compliance of the dural seal is a critical consideration for long-term multimodal interfaces. Furthermore, this interface shows the potential to overcome conventional localization limitations through early-stage visual co-registration. Although maintaining permanent optical clarity remains a fundamental challenge due to aggressive tissue responses, the system supports longitudinal high-density recording, providing a critical platform for multimodal studies bridging macroscopic network dynamics and microscopic cellular activity.

Keywords: electrocorticography; *Macaca mulatta*; Skull Window Techniques; Electrodes, Implanted; brain-computer interfaces

1. Introduction

Electrocorticography (ECoG) has emerged as a powerful modality for investigating neural activity, offering a compelling balance between spatial coverage, resolution, and signal quality. Positioned directly on the cortical surface, ECoG arrays circumvent the signal attenuation and spatial blurring inherent in non-invasive techniques like electroencephalography (EEG), while being less invasive than penetrating microelectrode arrays [1,2]. Furthermore, ECoG arrays have been shown to maintain long-term recording stability, making them highly suitable for chronic brain-machine interface (BMI) applications and longitudinal studies of cortical plasticity [3]. Recent advancements in microfabrication have led to the development of high-density micro-ECoG (μECoG) arrays, which possess the spatial resolution necessary to probe the brain's fine-scale functional architecture [4,5]. This technological leap opens up the possibility of resolving columnar-level or topographic organizations, such as color-selective modules in the visual cortex [6] or digit representations in the somatosensory cortex [7], which form the fundamental com-

putational units of the neocortex. Consequently, µECoG is becoming an increasingly vital tool, promising to deepen our understanding of cortical processing in basic neuroscience research and to enhance the performance of clinical applications such as pre-surgical mapping and next-generation brain-computer interfaces [8,9].

Realizing the full potential of high-density µECoG is, however, contingent upon overcoming a critical challenge: the uncertainty of electrode localization. For accurate signal interpretation, it is imperative to know precisely where on the cortical mantle each electrode resides. The conventional workflow provides essential estimates of placement by relying on intraoperative photographs and postoperative imaging like computed tomography (CT) or magnetic resonance imaging (MRI) [10,11]. This approach, however, is susceptible to significant inaccuracies, primarily due to brain shift—the physical displacement of the cortex that occurs both during and after surgery. The surgical act of opening the dura mater alters intracranial pressure and leads to cerebrospinal fluid drainage, causing the brain to deform and shift its position by several millimeters [12]. This degree of displacement significantly exceeds the sub-millimeter scale of cortical columns, rendering the subsequent mapping unreliable. Consequently, a spatial mismatch could potentially arise between the documented intraoperative placement and the actual final location of the array. This issue is further compounded by inaccuracies in the co-registration of postoperative images with the brain's anatomy [11,13,14]. Furthermore, brain volume and position are not static following surgery but can fluctuate chronically due to various physiological factors, such as changes in intracranial pressure, fluid dynamics, or physiological stress. Because of these ongoing volumetric changes, relying solely on intraoperative photographs taken before closing the surgical window, or terminal snapshots taken during explant, is fundamentally insufficient. Such static snapshots fail to capture the progressive displacements of the electrodes relative to the underlying cortex that may occur throughout the chronic recording period. Thus, a fundamental challenge persists: the invasive procedure required for high-resolution recording itself introduces substantial localization uncertainty, directly compromising the primary goal of precisely mapping neural activity to its cortical source.

The consequences of this localization uncertainty become particularly acute in studies aiming to integrate µECoG with high-resolution functional mapping techniques. Optical methods, from imaging of large-scale functional domains like orientation columns using intrinsic signals or voltage-sensitive dyes [15,16] to two-photon microscopy of single neurons [17], provide the detailed functional 'maps' of the cortex. The key scientific goal is to superimpose µECoG's electrical recordings onto these maps. This powerful multimodal approach, however, faces two fundamental challenges. First, it is critically dependent on precise spatial co-registration, which is rendered ambiguous by electrode localization uncertainty. Second, and perhaps more daunting for chronic multimodal studies, is the aggressive biological response of the primate brain. Chronic implantation typically induces severe dural regrowth and fibrous tissue encapsulation, rapidly obscuring optical access and altering the electrode-tissue interface. Therefore, to bridge the gap between high-resolution electrophysiology and functional imaging, a methodology is required that not only enables direct, continuous validation of electrode positions *in vivo*, but also effectively mitigates progressive tissue overgrowth to sustain long-term optical clarity.

To address these critical gaps, we have developed a chronic cranial window designed for direct, long-term visualization of an implanted µECoG array in primates. By replacing the native dura mater with a transparent glass window, this technique provides an unobstructed optical path to the cortical surface. Alongside ongoing advancements in electrode technologies, understanding how the biomechanical design of the dural interface influences chronic tissue responses remains a critical step for sustaining long-term optical access. Therefore, as the central focus of this study, we utilized a standard, electrically stable µECoG array to systematically compare two distinct dural interface designs—a floating Tecoflex sheet versus a bonded silicone ring. Through this comparison, we quantitatively characterize the spatiotemporal dynamics of post-surgical tissue responses, such as micro-hematomas and window opacification, alongside continuous impedance monitoring and the longitudinal tracking of functional signal degradation. Furthermore, we explore the potential of this transparent interface to facilitate early-stage spatial co-registration. By highlighting the critical mechanical and biological trade-offs involved, this work provides an essential foundational step toward bridging the gap between high-resolution electrophysiology and functional imaging. Additionally, this transparent interface permits continuous, non-invasive visual inspection of the tissue, providing contextual information for interpreting signal degradation and monitoring animal welfare.

2. Materials and Methods

2.1 Animals

Two adult male rhesus macaques (*Macaca mulatta*; 5–8 years old, weighing 7.8–9.2 kg), referred to as Monkey J and Monkey K, were used in this study. Monkey J was obtained from Anhui Deze Macaque Breeding Co., Ltd. (Xuancheng, Anhui, China), and Monkey K was obtained from Zhongke Lingrui (Zhanjiang) Biotechnology Co., Ltd. (Zhanjiang, Guangdong, China). The animals were housed in standard primate cages in an air-conditioned room maintained on a 14 h light/10 h dark cycle. They were provided with environmental enrichment and fed a standard primate diet supplemented with fruits and vegetables.

All procedures were conducted in accordance with the ARRIVE guidelines [18]; the completed ARRIVE checklist is provided in the **Supplementary Material**.

2.2 Anesthesia and Surgical Procedures

2.2.1 Surgical Anesthesia and Perioperative Care

All surgical protocols were conducted under standard aseptic conditions. Anesthesia was induced with an intramuscular injection of tiletamine-zolazepam (Zoletil 50; Carros, France; 2.5 mg/kg). The animals were then transported to the operating room, placed in a prone position, and secured in a stereotaxic head frame. Following induction, the animals were intubated and artificially ventilated (approximately 20–28 breaths/min, tidal volume ~13.5 mL/kg), and surgical anesthesia was maintained with 1.5%–2% isoflurane (Hebei Jindafu Pharmaceutical Co., Ltd., Xingtai, Hebei, China). Throughout the surgery, vital signs including blood oxygen saturation (SpO_2), end-tidal CO_2, heart rate, and core body temperature were continuously monitored. Body temperature was maintained at approximately 37 °C using a temperature-controlled water blanket (Stryker Medical, Portage, MI, USA). Prophylactic ceftriaxone sodium (Haikou Pharmaceutical Factory Co., Ltd., Haikou, Hainan, China) and dexamethasone (Shanghai Xiandai Hasen (Shangqiu) Pharmaceutical Co., Ltd., Shangqiu, Henan, China) were administered intramuscularly prior to surgery to prevent infection and reduce swelling. To manage peri-incisional pain, lidocaine (Jilin Huamu Animal Health Product Co., Ltd., Changchun, Jilin, China) was administered locally at the incision site.

Following surgery, animals were monitored closely until they recovered from anesthesia. Postoperative analgesia was provided for three days via twice-daily injections of buprenorphine (TIPR Pharmaceutical Co., Ltd., Tianjin, China; 0.005–0.010 mg/kg). Animals were provided oral hydration and a special diet of high-nutrition, easy-to-digest soft foods to promote recovery.

2.2.2 Anesthesia During Electrophysiological Recordings

During electrophysiological recording sessions, anesthesia was transitioned from isoflurane to a continuous intravenous infusion of propofol (Xi'an Libang Pharmaceutical Co., Ltd., Xi'an, Shaanxi, China; 2 mg/kg/h) and Zoletil 50 (1.5 mg/kg/h) to ensure a stable physiological state. The animal was simultaneously paralyzed with vecuronium bromide (Cisen Pharmaceutical Co., Ltd., Jining, Shandong, China; 0.05–0.1 mg/kg/h) to prevent eye movements. Throughout the sessions, heart rate, SpO_2, and $EtCO_2$ were continuously monitored to maintain a consistent and adequate depth of anesthesia.

2.3 µECoG Array

The µECoG array used in this study was a 64-channel, high-density grid (Model E64-1000-50-200, NeuroNexus, Inc., Ann Arbor, MI, USA). The array consisted of platinum electrode contacts, each 200 µm in diameter, arranged in an 8 × 8 grid with a center-to-center distance of 1 mm. The contacts were embedded in a 20-µm thick, flexible polyimide substrate. This substrate is transparent and biocompatible, allowing for gentle conformity to the cortical surface while maintaining optical access.

2.4 Chronic Cranial Window Assembly

The chronic cranial window was a custom-fabricated, multi-component chamber providing stable optical access to the implanted µECoG array and the cortical surface. The assembly comprised three primary components: a PEEK (polyether ether ketone) chamber body, an optically transparent glass window, and a flexible dural-interfacing ring (Fig. 1).

2.4.1 Chamber Body and Optical Window

The main structural body (chamber, Item 7 in Fig. 1) was fabricated from black PEEK, a medical-grade thermoplastic designed to fit securely within the craniotomy. Its external flange was anchored to the skull (Item 5) using dental cement (Anyang Yingpai Dental Material Co., Ltd., Anyang, Henan, China; Item 6) to isolate the viewing area. A circular glass coverslip (Item 4) was hermetically sealed to the bottom of the chamber, providing an unobstructed optical path for imaging and localization of the µECoG electrodes relative to cortical vascular landmarks.

2.4.2 Dural Interface Design

To prevent cerebrospinal fluid (CSF) leakage and impede tissue overgrowth—the primary cause of window opacification—a flexible ring was positioned at the interface between the chamber and the dura mater (Item 2). We employed two different designs across the subjects to optimize long-term visibility. Both designs utilized a standardized chamber assembly featuring an outer diameter of 23 mm and an inner glass window diameter (visible area) of 18 mm.

Design 1: In the first subject (Monkey J), a 0.005-inch-thick (approximately 0.127 mm) Tecoflex sheet (EG-93A, Lubrizol Advanced Materials, Wilmington, MA, USA; Item 3) was used. This thermoplastic polyurethane was selected based on our established success using it in chronic imaging chambers [6], as well as for its high optical clarity, biocompatibility, and "in-body softening" characteristics, which effectively damp cortical pulsations and minimize tissue trauma. The sheet was placed underneath the chamber without chemical bonding, and a mechanical seal was created by tucking its outer edge under the native dura (Item 2).

Design 2: To achieve a more robust and airtight seal, the design was modified for the second subject (Monkey K). A 0.1-mm-thick silicone sheet ring (Item 3) was permanently bonded to the glass coverslip using a silicone adhesive (KE-1300T and CAT-1300; Shin-Etsu Chemical,

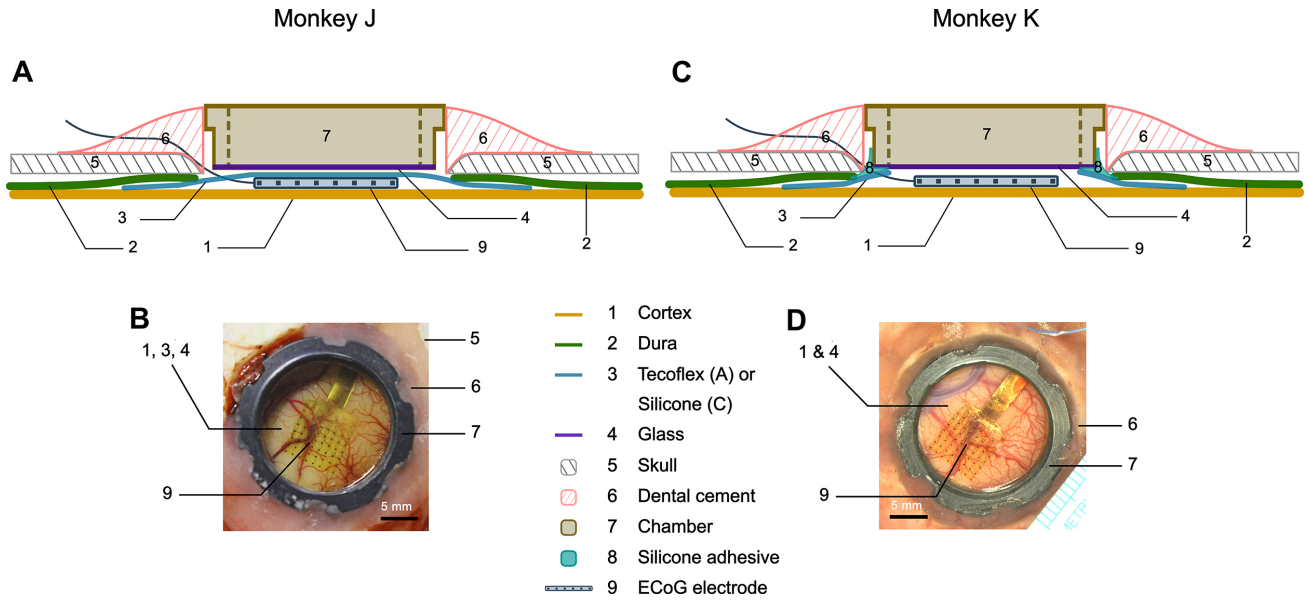

Fig. 1. Design and surgical implantation of the chronic optical window for micro-electrocorticography (µECoG) arrays. (A,B) Optical window Design 1 evaluated in Monkey J. (A) Schematic cross-section. A Tecoflex sheet (3) is placed directly beneath the glass window (4) and secured solely by mechanical pressure from the chamber (7), without chemical bonding. (B) Photograph showing the implantation of Design 1. (C,D) Optical window Design 2 evaluated in Monkey K. (C) Schematic cross-section. A silicone ring (3) is bonded to the glass window (4) and the chamber (7) with silicone, forming a robust, hermetic seal. (D) Photograph showing the implantation of Design 2. Scale bars in (B) and (D) represent 5 mm.

Tokyo, Japan). Silicone was specifically selected for this peripheral sealing component due to its mechanical versatility and its reliable capacity to form a hermetic bond with the chamber assembly, rather than for its optical properties. During implantation, the outer edge of this silicone ring was tucked underneath the cut edge of the native dura (Item 2), creating a physical barrier to the ingrowth of dural tissue.

2.5 Surgical Implantation Procedures

The localization of the craniotomy was determined intraoperatively based on skull landmarks, such as cranial sutures, targeting the lateral end of the lunate sulcus—a region that typically includes visual cortical areas V1, V2, and V4. To ensure precise exposure of the target regions, a limited durotomy was first performed to visually confirm the anatomical position of the sulcus. Guided by this direct observation, the craniotomy was subsequently extended as necessary.

The implantation procedure was conducted as follows. First, the skin over the target area was incised to expose the skull, and a bone flap of approximately 3–4 cm in diameter was removed using a dental drill (RWD Life Science Co., Ltd., Shenzhen, Guangdong, China). The dura mater was carefully incised and retracted to expose a 2–3 cm area of the cortical surface, onto which the µECoG array was gently placed. The subsequent steps for sealing the craniotomy varied depending on the dural interface design. For Design 1, a Tecoflex sheet was tailored to fully cover the exposed cortex. To allow the flat electrode cable to exit the subdural space, a small slit was cut into the edge of the sheet. The sheet was placed over the array, the flat cable was routed outward through this slit, and the sheet's periphery was carefully tucked under the native dural margins. The chamber with the glass window was then positioned over the sheet, maintaining a clear view of the array. For Design 2, the chamber was positioned directly over the array without the Tecoflex sheet. To accommodate the exiting flat electrode cable, a slit was made in the silicone ring bonded to the chamber base. Additionally, the ring was tailored to fully cover the exposed cortex. The cable was routed through the slit, and the silicone ring was subsequently tucked under the outer dural edges.

Following the placement of the chamber, three to four bone screws were implanted into the surrounding skull to serve as anchors. A platinum reference electrode was inserted subdurally adjacent to the craniotomy. Dental cement was applied around the chamber base, anchoring it firmly to the skull and screws to create a stable, watertight assembly. The externalized portion of the electrode cable, the ECoG connector port, and a custom connector box were entirely embedded and secured within the dental cement. Finally, the skin was sutured tightly around the base of the secured chamber assembly, ensuring that no skull bone remained exposed.

2.6 Quantification of Electrode Displacement

To quantify electrode displacement following implantation, we established an image registration and displace-

ment measurement protocol. Vascular intersection points clearly visible across all imaging sessions (Day 0, Day 7, and Day 14) were selected as fiducial markers. Using the post-implantation image at Day 0 as the reference, optimal perspective transformation matrices were estimated via a least-squares fitting approach implemented in custom MATLAB scripts in MATLAB R2024a (MathWorks, Natick, MA, USA). This transformation registered images from subsequent time points (Day 7 and Day 14) to the Day 0 coordinate system, correcting for global geometric distortions caused by variations in camera viewing angle. Following registration, the center coordinates of each electrode were manually identified using Adobe Photoshop 2024 (version 25; Adobe Inc., San Jose, CA, USA) at a spatial resolution where 1 mm corresponded to 125 pixels (equivalent to 8 µm/pixel). The Euclidean distance between the electrode positions at Day 7/14 and their baseline positions at Day 0 was calculated. Outliers were identified using Tukey's method, defined as values exceeding 1.5 times the interquartile range (IQR) from the upper or lower quartiles.

2.7 Visual Stimulation

Visual stimuli were generated using a ViSaGe MKII visual stimulus generator (Cambridge Research Systems, Rochester, UK) controlled by custom software written in MATLAB utilizing the CRS Toolbox. Stimuli were displayed on a 27-inch LCD monitor (272G5DJEB; Philips, Amsterdam, Netherlands) with a resolution of 1920 × 1080 pixels and a refresh rate of 60 Hz. The monitor was positioned 57 cm from the animal's eyes. The pupils were dilated with atropine sulfate (Anhui Changjiang Pharmaceutical Co., Ltd., Wuhu, Anhui, China; 0.5 mg/mL) and custom-made contact lenses (Autek China Inc., Hefei, Anhui, China) with appropriate curvature were fitted to focus the eyes at this viewing distance. Monitor luminance and color output were gamma-corrected using a SpectroCAL MKII spectroradiometer (Cambridge Research Systems, Rochester, UK). To achieve monocular stimulation, one eye was manually occluded using aluminum foil. Data collection followed a block design in which the occluded eye was switched every 40 trials, while the presentation order of visual stimuli within each block was pseudo-randomized. The display background was a uniform gray field maintained at a mean luminance of 35 cd/m^2.

The primary stimuli consisted of full-screen drifting sinusoidal gratings with a spatial frequency (SF) of 1.5 cycles/degree and a temporal frequency (TF) of 2 Hz (drift speed: 2 cycles/s). The spatial phase of the grating was randomized (0–360°) for each presentation. Two stimulus chromaticities were used: (1) isoluminant red/green gratings and (2) 100% luminance-contrast black/white gratings. Both stimulus types were matched in mean luminance to the background (35 cd/m^2). The gratings were presented at two orientations (horizontal and vertical) and drifted in directions perpendicular to their orientation. Each trial comprised a 0.5 s pre-stimulus period (gray background), followed by a 3.5 s visual stimulus presentation, and concluded with a 5.0 s post-stimulus period (gray background).

2.8 Data Acquisition

Neural signals were acquired using custom-configured 256-channel data acquisition system comprising an RZ2 Z-Series processor, a PZ5M-256 Z-Series 256-channel neurodigitizing preamplifier, and an RS4 Z-Series data streamer (Tucker-Davis Technologies, FL, USA). The signals were differentially amplified referenced to the subdural platinum electrode, bandpass filtered online (0.5–200 Hz), and digitized at a sampling rate of 3 kHz. To reduce computational load, all data were downsampled to 500 Hz prior to analysis. Electrode impedance was measured at 1 kHz using the same system in Monkey K. Because the systematic impedance monitoring protocol was integrated into our workflow only after the initial experiments, these measurements were not collected for the first subject (Monkey J). Recording sessions involving visual stimulation were performed periodically. Note that for Monkey K, impedance monitoring was continued up to Day 42, while functional data acquisition with visual stimulation was concluded on Day 28 due to the experimental schedule.

2.9 Data Analysis

2.9.1 Signal Preprocessing

Raw ECoG signals were preprocessed using the FieldTrip toolbox (fieldtrip-20240110; developed and maintained at the Donders Institute for Brain, Cognition and Behaviour, Radboud University, Nijmegen, The Netherlands; https://www.fieldtriptoolbox.org/) [19] and custom MATLAB scripts, following established protocols in our laboratory [20]. First, the signals were digitally filtered with a band-pass filter (0.5–200 Hz) and a notch filter (50 Hz) to remove direct-current (DC) offsets, slow drifts, and power-line noise. All signals were then resampled to 500 Hz to reduce the computational load while maintaining a sufficient Nyquist frequency for the high-frequency components of interest. To remove global noise and enhance the signal-to-noise ratio, all channels were re-referenced using a common average reference (CAR). Finally, non-neural physiological artifacts were identified and mitigated using independent component analysis (ICA) via the Infomax algorithm implemented in FieldTrip. Consistent with our established protocol, which typically removes 3–4 noise components from 192-channel recordings [21], a proportionally small number of components (1–2 out of 64) clearly representing artifacts were identified by visual inspection of their waveforms and topographic maps and were subsequently removed before reconstructing the signals.

2.9.2 Visual Evoked Potential (VEP) Analysis

To evaluate phase-locked neural responses to visual stimulation, visual evoked potentials (VEPs) were calculated. Preprocessed ECoG signals were segmented into epochs ranging from −1.0 to +4.5 s relative to the stimulus onset. To preserve trial-to-trial amplitude variability while standardizing the signal scale across channels, baseline correction (z-score normalization) was applied using pooled baseline statistics. Specifically, for each electrode channel, the mean and standard deviation of the voltage were calculated by pooling the pre-stimulus baseline data (−1.0 to −0.5 s) across all trials within a recording run. Each epoch was then normalized by subtracting this common baseline mean and dividing by the common standard deviation. VEP waveforms were finally derived by trial-averaging these z-scored segments for each stimulus condition and electrode channel.

2.9.3 Time-Frequency Analysis

To investigate the spectral dynamics of induced neural activity, time-varying power spectra were estimated using a wavelet transformation provided by the FieldTrip Toolbox. The analysis covered a frequency range of 1 to 100 Hz. For visualization of time-frequency representations, power was calculated based on the z-score normalized signals described above. To evaluate stimulus-induced power changes, the mean power during the pre-stimulus baseline period (−1.0 to −0.5 s) was subtracted from the resulting spectrograms. To compensate for the 1/f spectral decay and facilitate the visualization of high-frequency components, the power spectra were multiplied by their respective frequencies (spectral whitening). The resulting time-frequency representations are expressed in arbitrary units (a.u.) reflecting the whitened spectral power of the normalized signals. For the quantitative analysis of gamma-band power, power was calculated from unnormalized signals. Gamma-band power (30–80 Hz) at 0.5 s after stimulus onset was baseline-corrected by subtracting the mean power during the pre-stimulus period (−1.0 to −0.5 s). To visualize the spatial distribution of these functional responses across the cortex, the baseline-corrected gamma-band power values (30–80 Hz) were further normalized to the maximum absolute value within each recording session. These normalized values were then mapped onto the electrode grid geometry to generate topographic maps, allowing for direct comparison of spatial patterns across different recording sessions and subjects.

2.9.4 Neural Decoding Analysis

To evaluate the stability of visual information representation throughout the chronic implantation period, we conducted a neural decoding analysis using a multivariate pattern analysis (MVPA) approach based on our previously established methods [20]. We focused on discriminating between the two stimulus chromaticities described in Section 2.7—isoluminant red-green (RG) and 100% luminance-contrast black-white (BW) gratings—independently for each recording session to track longitudinal changes in classification accuracy. Decoding features were constructed from the time-frequency representation of ECoG signals; specifically, gamma-band (30–80 Hz) spectral power was calculated using a wavelet transform with a 0.5-s analysis window. To capture the complete spatiotemporal dynamics of the neural response, gamma power values were extracted from eight time points (0, 0.5, 1.0, 1.5, 2.0, 2.5, 3.0, and 3.5 s relative to stimulus onset) covering the entire 3.5-s stimulus presentation period, and these values across all valid electrode channels were concatenated into a single high-dimensional feature vector for each trial (e.g., 64 channels × 8 time points). We employed a linear support vector machine (SVM) classifier implemented via the LIBLINEAR toolbox [22] in MATLAB and evaluated performance using a 10-fold cross-validation scheme, averaging accuracies across folds where nine subsets were used for training and one for testing. Statistical significance against the chance level (50%) was assessed using a bootstrap test with 1000 iterations, and 95% confidence intervals were calculated to estimate the reliability of the decoding accuracy.

3. Results

To validate the stability and efficacy of our novel chronic cranial window assembly for high-density microelectrocorticography (μECoG), we performed implantation surgeries on two macaque monkeys (Monkey J and Monkey K).

3.1 Chronic Maintenance of Optical Clarity for Cortical Monitoring

To establish long-term, stable optical access to the implanted μECoG array and the underlying cortex, it is essential to mitigate the progressive opacification typically caused by dural tissue invasion. To address this, we evaluated the efficacy of two distinct optical window designs in maintaining window transparency over time (Fig. 1). Design 1, tested in Monkey J, utilized a Tecoflex sheet (Fig. 1A,B, item 3) placed directly beneath the glass window under pressure, without chemical bonding. In contrast, for Monkey K, we utilized Design 2 featuring a silicone ring (Fig. 1C,D, item 3)—bonded to the glass window and chamber with silicone and tucked under the native dural edge—to create a robust, hermetic seal. The longitudinal performance of these designs was assessed through periodic microscopic monitoring of the cortical field of view and electrode visibility (Fig. 2).

In Monkey J, high optical clarity was preserved through Day 7, and clear identification of electrode contacts relative to the cortical vasculature remained possible on Day 14 (Fig. 2C,D). However, subsequent weeks revealed a progressive ingrowth of opaque tissue, encroaching from

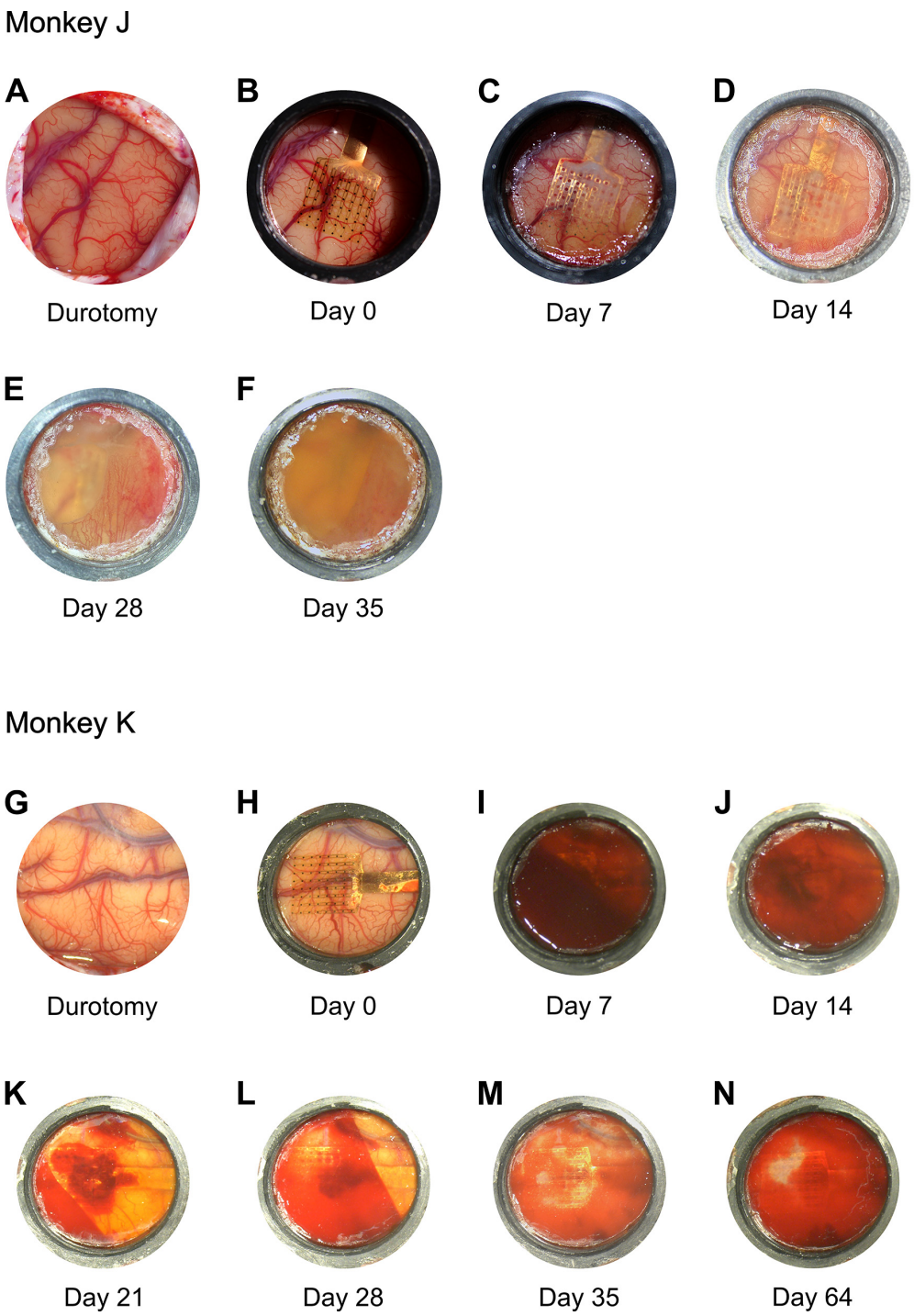

Fig. 2. Longitudinal assessment of optical clarity and electrode visibility across dural interface designs. (A–F) Serial photographs of the cranial window in Monkey J (Design 1) at different stages: durotomy (before implantation), Day 0 (immediately after implantation of the electrode array and chamber assembly), and Days 7, 14, 28, and 35 post-implantation. (G–N) Serial photographs of the cranial window in Monkey K (Design 2) at corresponding stages: durotomy, Days 0, 7, 14, 21, 28, 35, and 64 post-implantation. The center-to-center distance between adjacent electrodes is 1 mm.

the chamber periphery toward the center (Fig. 2D,E). By Day 35, this centripetal opacification had obscured the majority of the array (Fig. 2F).

In Monkey K, a subdural hemorrhage occurred immediately following implantation, likely originating from the dural edge (Fig. 2I). This resulted in the initial formation of a hematoma beneath the glass window, occluding the view of both the cortex and the array. Although this hematoma

persisted for over a month, the blood began to clear by Day 21, successfully restoring visibility of the µECoG array and portions of the underlying cortex (Fig. 2K). However, the hematoma remained without disappearing completely, and by Day 64, it had come to cover most of the glass window. Notably, despite the presence of the hematoma, the invasion of fibrotic tissue from the periphery, which was observed in Monkey J, was not observed in Monkey K up to Day 35.

The presence of the optical window proved advantageous in both scenarios. It enabled the early detection of postoperative hemorrhage and the continuous, non-invasive monitoring of tissue responses. This capability provided critical insights into the status of the intracranial environment, which would remain concealed in standard non-transparent implantations.

3.2 Quantification of Electrode Displacement

Leveraging the preserved optical clarity in Monkey J up to Day 14, we quantitatively evaluated the spatial stability of the µECoG array by monitoring its physical displacement relative to vascular landmarks. A quantitative analysis of the displacement of electrodes (n = 64) relative to the baseline position at Day 0 revealed a slight but progressive shift (Fig. 3). The median displacement was 0.12 mm (IQR: 0.10–0.14 mm) at Day 7 and increased to 0.20 mm (IQR: 0.14–0.23 mm) by Day 14. By this endpoint, the displacement corresponded to approximately 20% of the 1.0 mm inter-electrode spacing. Crucially, the optical window permitted the precise tracking of these sub-millimeter movements, validating the physical stability of the array.

3.3 Functional Validation of µECoG Recordings

Having confirmed the optical visibility and physical stability of the implant, we next sought to validate the electrophysiological performance of the µECoG array. We assessed the longitudinal quality of the neural recordings by analyzing electrode impedance, spectral response characteristics, and the stability of functional mapping.

3.3.1 Longitudinal Stability of Electrode Impedance

To validate the electrochemical performance of the chronic window assembly, we monitored electrode impedance in Monkey K over a six-week period (Fig. 4). As noted in the Methods, this longitudinal monitoring was only implemented for the second subject. On the day of implantation (Day 0), the electrodes exhibited low impedance values (median 16.8 kΩ; IQR 15.3–18.8 kΩ), indicating clean contact with the cortical surface. By Day 7, impedance increased markedly (median 79.8 kΩ; IQR 64.0–92.5 kΩ). In this subject, the subdural hematoma described in Section 3.1 likely further contributed to this acute change in the electrical interface. Following this initial phase, impedance values plateaued and remained relatively constant from Day 14 through Day 42, fluctuating within a stable functional range (median 59.7–74.6 kΩ).

To address the spatial dynamics of the electrical interface, we mapped the impedance values topographically (Fig. 4B). Throughout the six-week period, the majority of the array maintained stable impedance levels. At Day 0, four channels exhibited impedances exceeding 200 kΩ (masked in gray as high-impedance outliers in Fig. 4B). While three of these remained persistently high—potentially indicating initial micro-mechanical damage to the traces during surgical handling—other outliers fluctuated transiently across sessions. By Day 42, three channels exceeded 200 kΩ, leaving approximately 95% (61/64) of the array within the typical stable range. These transient regional fluctuations and the late emergence of a few high-impedance channels likely reflect the dynamic progression of the underlying subdural hematoma (e.g., clot retraction and lysis) and localized micro-encapsulation driven by inflammatory responses to blood products. While stable impedance alone does not definitively confirm persistent physical contact with the cortical surface due to the potential conductivity of reactive tissue, these longitudinal observations provide an initial demonstration that the electrical interface remained functional within a stable range throughout the chronic period.

3.3.2 Temporal and Spectral Characteristics of Visual Responses

To verify that the signals reflected physiological neural activity, we analyzed both the time-domain and frequency-domain characteristics of the responses to red-green grating stimuli. In the time domain, trial-averaged waveforms across the array typically exhibited attenuated VEPs (Fig. 5A). This relative lack of prominent VEP amplitude is a predicted outcome of our recording configuration and signal processing paradigm. Specifically, the use of a local subdural reference electrode positioned adjacent to the array and the subsequent application of a CAR effectively subtracts spatially synchronized, common-mode low-frequency components that are distributed across the visual cortex. However, this configuration is optimized for extracting local, non-phase-locked high-frequency activity. As shown in the magnified waveform from an example channel, distinct high-frequency fluctuations were superimposed on the attenuated potential during the stimulus period (Fig. 5B). In addition to the time-domain waveforms, time-frequency analysis was used to assess functional responses across sessions. As visualized in the grid-wide spectrograms, visual stimulation elicited broadband spectral power increases across the majority of channels immediately following stimulus onset (Fig. 5C). A closer examination of the corresponding spectrogram demonstrates a prominent and sustained elevation in power across a wide frequency range, spanning alpha, beta, and gamma bands, confirming the presence of strong visual responses despite the attenuated VEP amplitude (Fig. 5D).

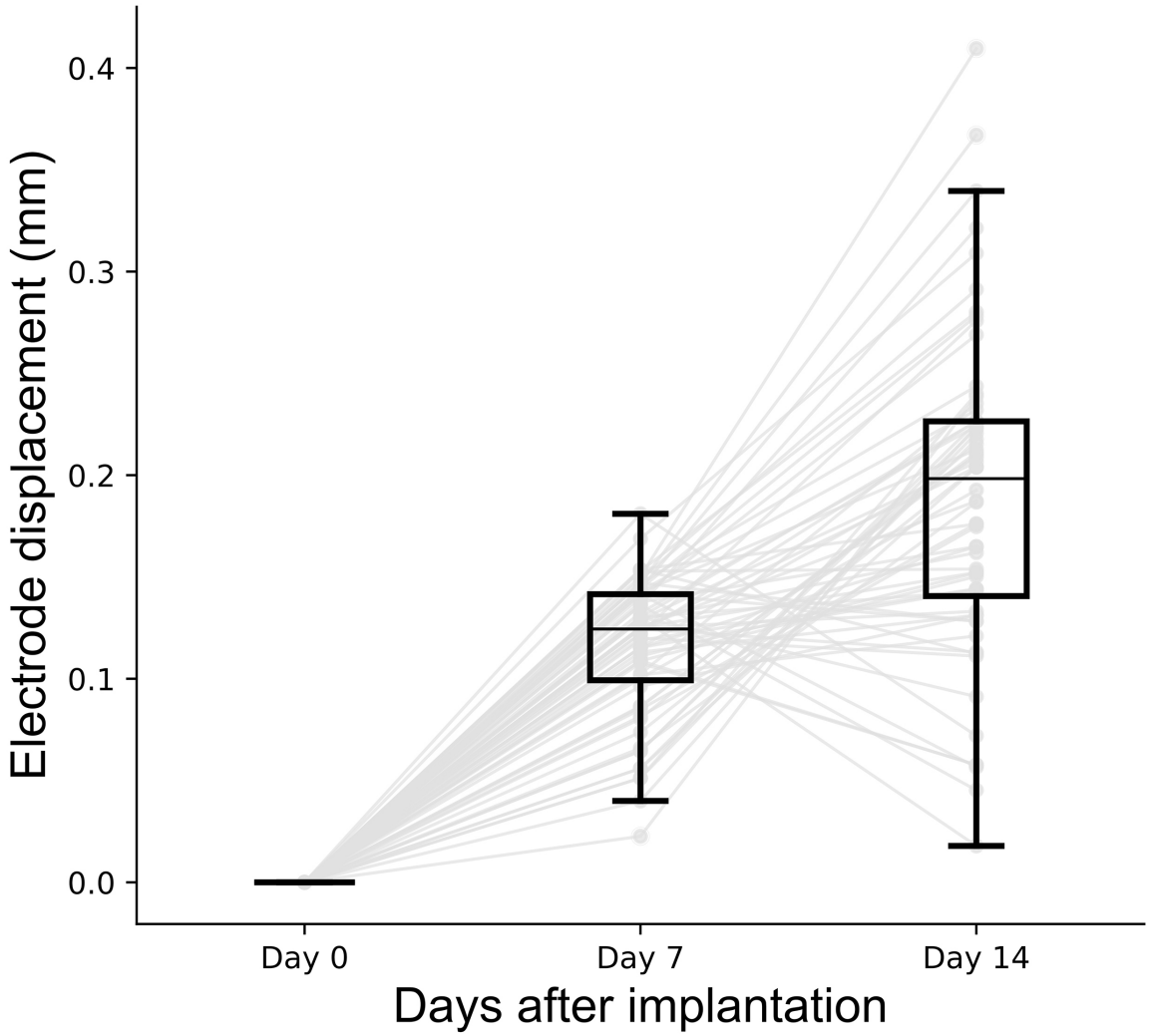

Fig. 3. Quantification of physical electrode migration (Monkey J). Time course of electrode displacement relative to the baseline position at Day 0. The box plots summarize the distribution of displacement values across 64 electrodes in Monkey J (one animal). The central line within each box indicates the median. The bottom and top edges of the box indicate the 25th and 75th percentiles (interquartile range; IQR), respectively. Whiskers extend to the most extreme data points within 1.5 × IQR (Tukey's method). Individual electrode trajectories are shown as grey lines and points.

Longitudinal assessment across all channels and sessions provided a comprehensive overview of these functional responses (Fig. 6). In Monkey J, spectral power increases were observed across the grid during the early to intermediate phases (Days 14 and 35). In later sessions (Days 154 and 172), these responses tended to be more localized or attenuated, which may be related to the progression of dural tissue regrowth over the chronic period. Conversely, Monkey K initially showed restricted responses (Days 7 and 14), which appeared to expand across more channels in subsequent sessions (Days 21 and 28). These comprehensive observations clearly demonstrate that the spatial distribution and magnitude of the functional signals dynamically change over time.

3.3.3 Longitudinal Dynamics of Gamma-Band Responses

We characterized the spatiotemporal dynamics of induced gamma-band power (30–80 Hz) to evaluate the functional integrity of the µECoG interface over time. We focused on this frequency range because gamma-band activity is known to be localized and closely correlated with local neuronal spiking, making it an ideal metric for functional mapping with high spatial resolution [23,24]. As shown in the topographic maps (Fig. 7A), visual stimulation elicited increases in gamma power within the visual cortical area covered by the array across recording sessions. To provide a quantitative measure of functional yield, we identified individual channels exhibiting statistically significant power increases relative to the pre-stimulus baseline (indicated by white stars). We tracked these functional visual responses

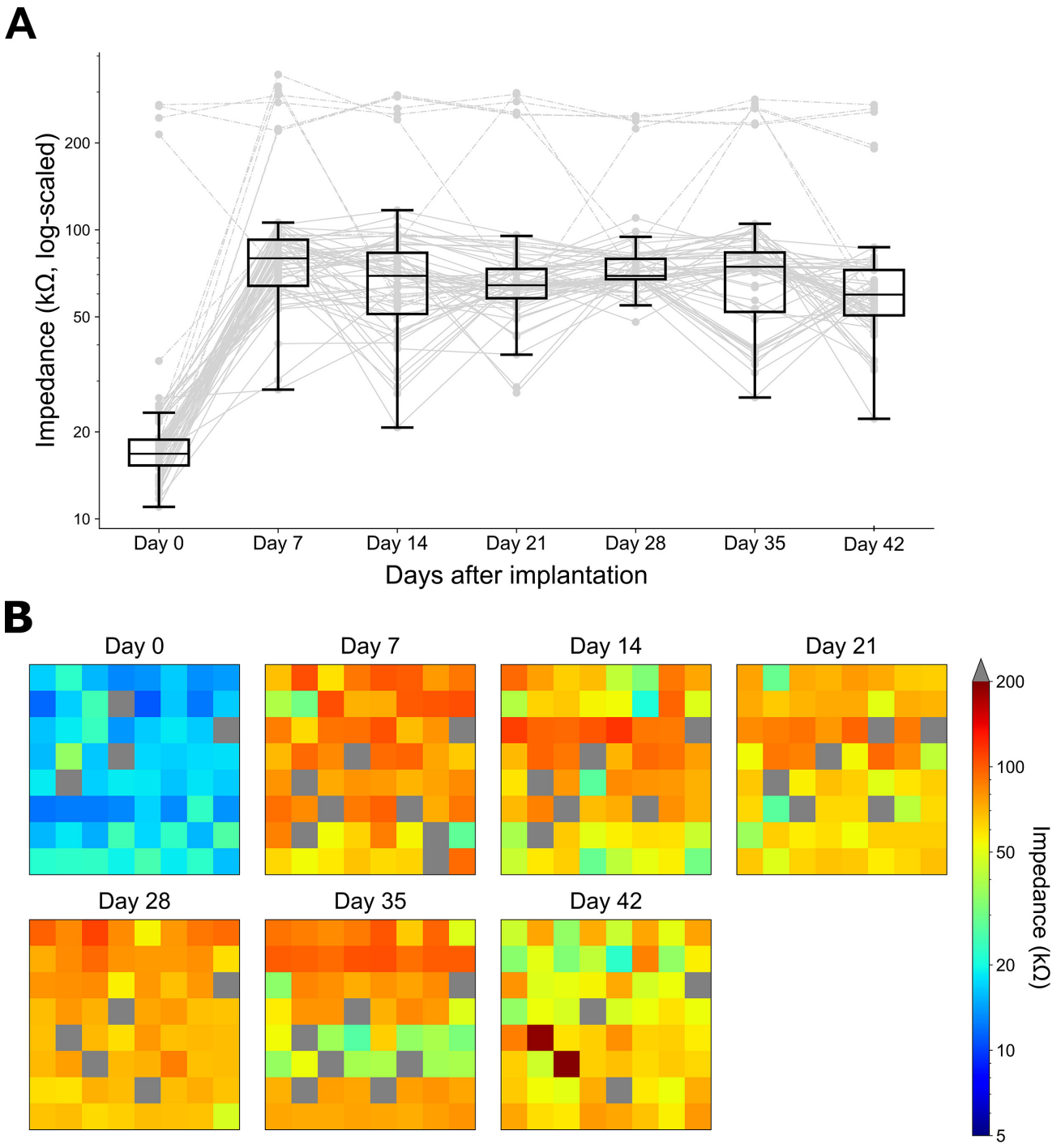

Fig. 4. Longitudinal stability of electrode impedance (Monkey K). (A) Time course of electrode impedance (magnitude at 1 kHz) measured for all 64 electrodes over a six-week period. The box plots summarize the distribution of impedance values at each time point. Box plot conventions are identical to Fig. 3. (B) Topographic heatmaps illustrating the spatial distribution of electrode impedances across the array for each recording session. The color scale represents the impedance magnitude. Channels exhibiting impedances exceeding 200 kΩ are masked in gray as high-impedance outliers.

across the chronic implantation period, with final observations occurring at Day 172 for Monkey J and Day 28 for Monkey K.

The topographic configuration (Fig. 7A) and overall magnitude (Fig. 7B) of these gamma responses exhibited noticeable variability across sessions. To quantitatively estimate the electrophysiological performance over time, we calculated the percentage of functionally relevant channels (marked with white stars in Fig. 7A). In Monkey J, widespread significant responses were observed initially,

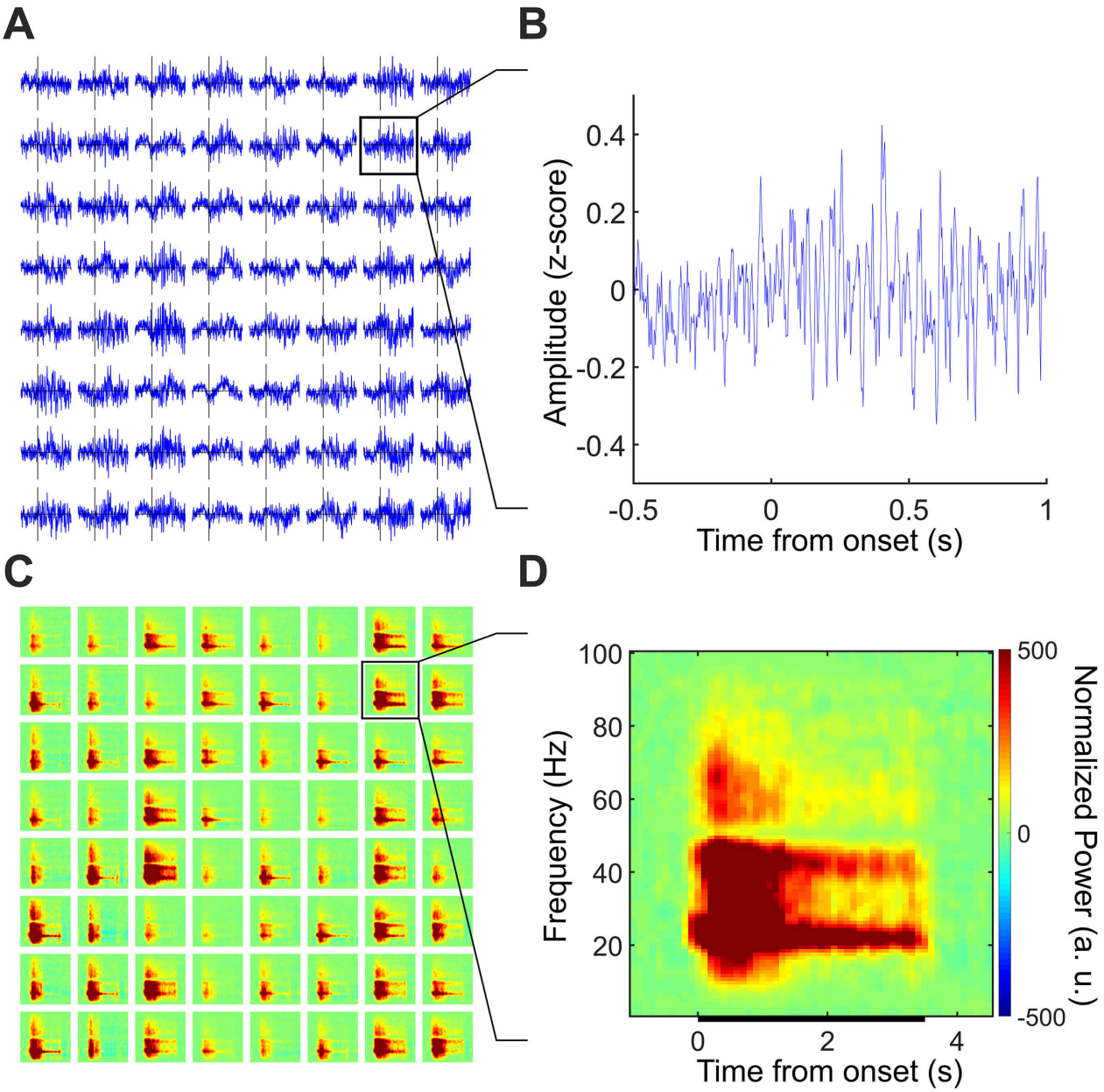

Fig. 5. Example electrophysiological responses to visual stimulation (Monkey J). (A) Grid-wide plot of visual evoked potentials (VEPs) elicited by red-green grating stimuli, averaged across 181 trials from a single recording session (Day 14). Each subplot represents the signal from one electrode channel arranged topographically. (B) Magnified view of the averaged VEP waveform from an example channel (indicated by the box in A). The y-axis represents amplitude normalized as z-scores relative to the pre-stimulus baseline. (C) Grid-wide time-frequency spectrograms showing spectral power changes relative to stimulus onset. Warmer colors indicate increases in power. (D) Magnified view of the spectrogram from the same channel as in B. Color scale represents normalized spectral power (arbitrary units [a.u.]), frequency-weighted to compensate for 1/f decay. The black bar along the x-axis indicates the duration of the visual stimulus. The narrow reduction in power at 50 Hz corresponds to the notch filter applied for line noise removal. For a full overview of functional responses across all sessions and channels, see Fig. 6.

with 100% (64/64 channels) and 98% (63/64 channels) demonstrating functional modulation at Days 14 and 35, respectively. However, during the extended chronic phase, overall gamma power was drastically reduced; on Day 154, no channels (0%) met the criterion for statistical significance, though 16% (10/64 channels) recovered significant responses by Day 172 (over 5 months). Conversely, Monkey K initially showed restricted significant responses, with only 16% (10/64 channels) and 20% (13/64 channels) exhibiting significant modulation during the acute phase

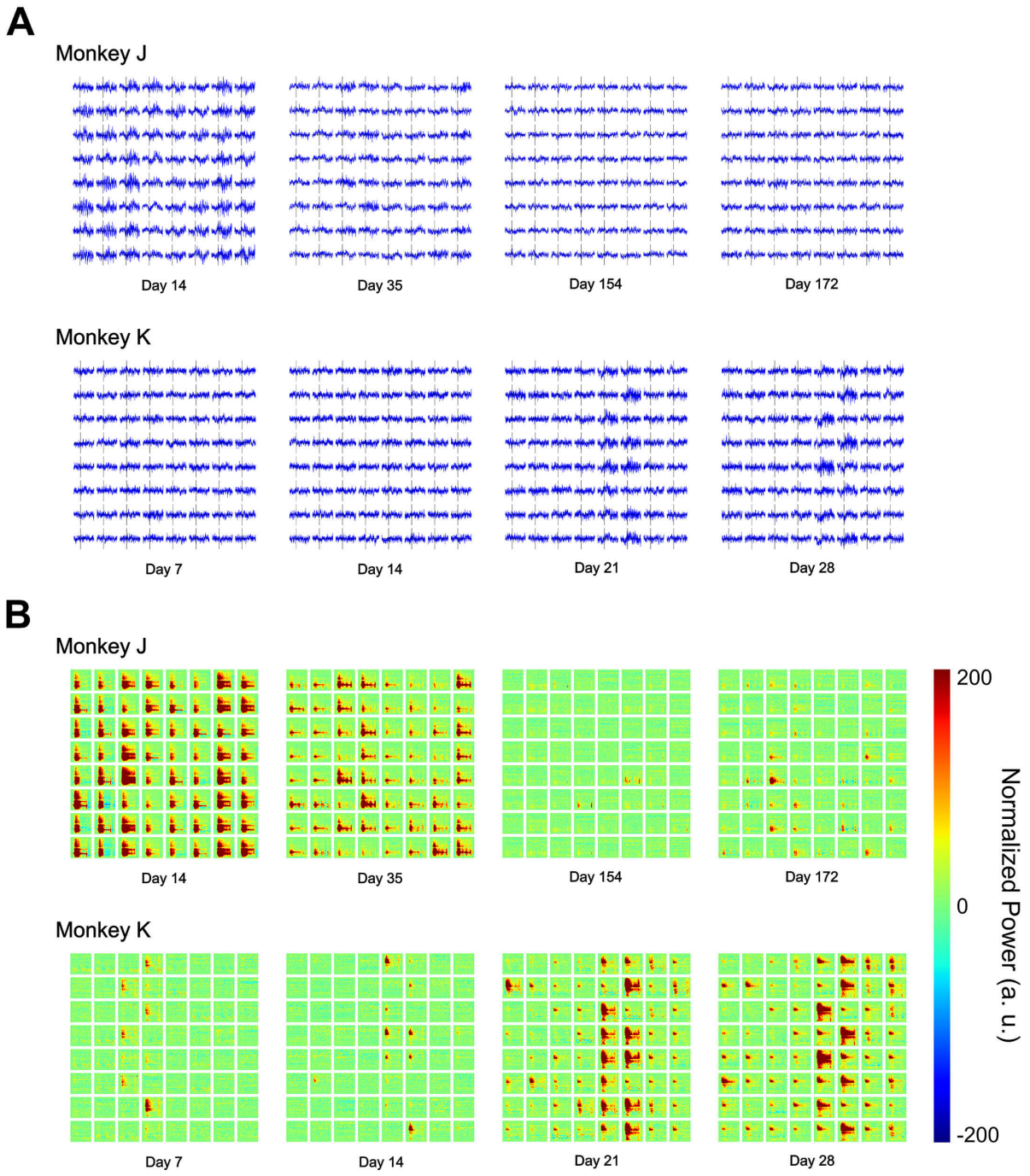

Fig. 6. Longitudinal grid-wide functional responses across all electrode channels. (A) Topographic plots of VEPs for Monkey J (Days 14, 35, 154, and 172) and Monkey K (Days 7, 14, 21, and 28). The plotting format for each session follows that of the example in Fig. 5A. (B) Grid-wide time-frequency spectrograms for the same sessions shown in (A). The plotting format for each session follows that of the example in Fig. 5C, except for the color scale (Z-range), which is standardized across all sessions as indicated by the color bar on the right. The total number of trials per session was 181, 192, 223, and 189 for Monkey J (Days 14, 35, 154, and 172) and 153, 130, 155, and 184 for Monkey K (Days 7, 14, 21, and 28), respectively.

(Days 7 and 14). In subsequent sessions, these responses expanded, and recordings spanning up to Day 28 (approximately 1 month) demonstrated significant power increases in 94% (60/64 channels) and 91% (58/64 channels) at Days 21 and 28, respectively.

These variations in response patterns and signal magnitude likely reflect a combination of factors. The attenuation in Monkey J may be related to the progressive physical separation of the grid caused by dural tissue regrowth over the chronic period, potentially compounded on specific

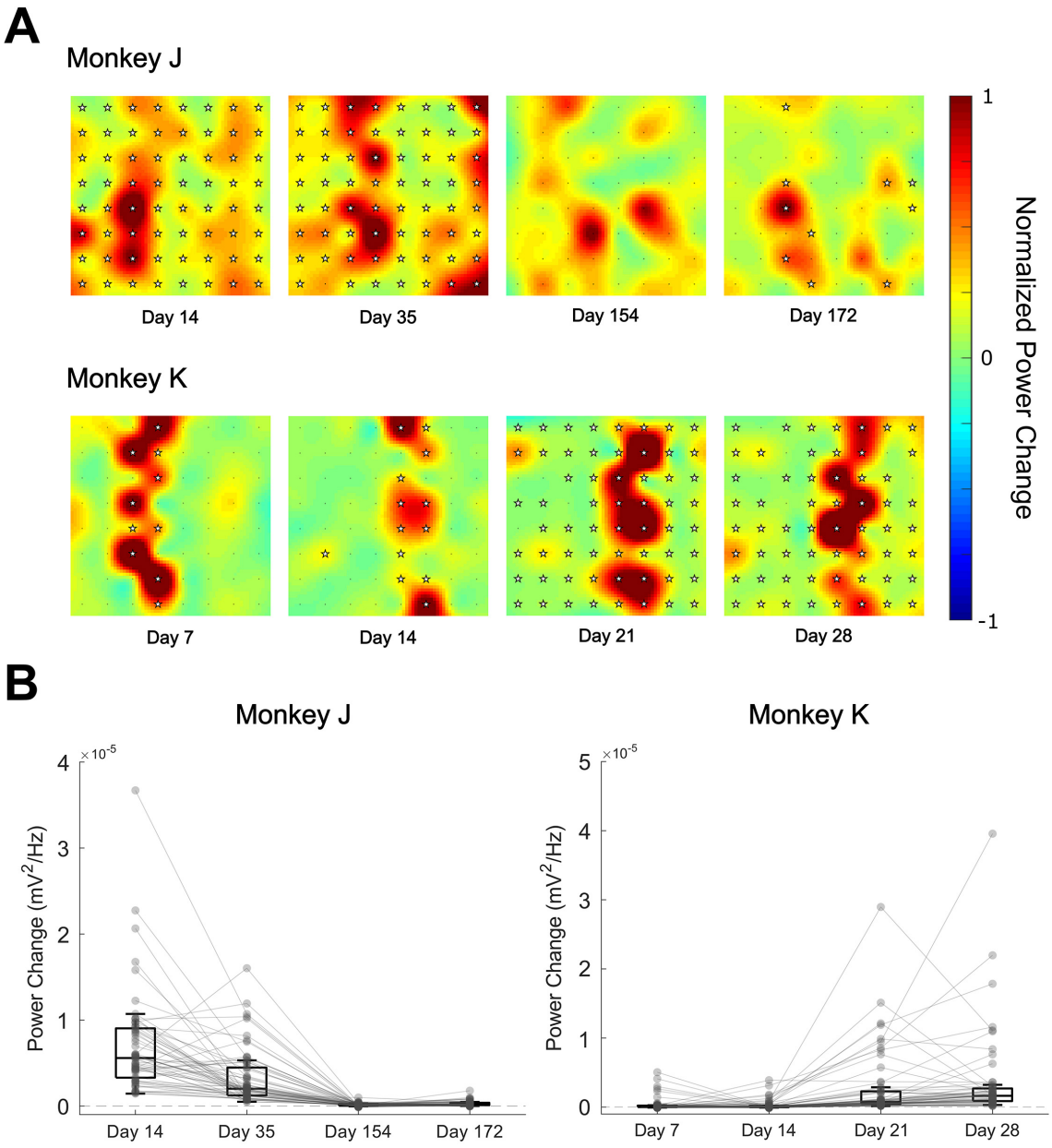

Fig. 7. Longitudinal assessment of gamma-band response characteristics. (A) Topographic maps of gamma-band power (30–80 Hz) responses to red-green grating stimuli for Monkey J (upper row) and Monkey K (lower row). Each panel displays the spatial distribution of spectral power at 0.5 s after stimulus onset. The color scale represents the spectral power normalized to the maximum absolute value within each recording session to allow for the direct comparison of spatial topographies across days. White stars indicate individual channels exhibiting a statistically significant increase in gamma power relative to the pre-stimulus baseline (two-sided paired *t*-test with false discovery rate (FDR) correction, $p < 0.05$). (B) Longitudinal dynamics of response magnitude. Box plots summarize the distribution of gamma-band power changes (30–80 Hz) across all 64 channels, measured at 0.5 s post-stimulus onset for each recording session. Grey lines connect individual channels across sessions, illustrating the longitudinal trajectories of power changes over time. Plotting conventions for the box plots are identical to those in Fig. 4A. Trial counts for each session are identical to those specified in the legend of Fig. 6. Note that while impedance monitoring continued up to Day 42 for Monkey K (Fig. 4), visual stimulation sessions were concluded on Day 28 due to the experimental schedule.

days (e.g., Day 154) by extrinsic factors such as session-specific anesthetic depth. In contrast, the expansion of responsive channels in Monkey K might be associated with the gradual resolution of the initial subdural hematoma and a corresponding improvement in electrode-cortical contact. These observations indicate that while functional signals

can be recorded over the long term, their spatial distribution and magnitude can change over time, potentially reflecting the evolving physical and physiological environment of the interface.

3.3.4 Longitudinal Performance of Visual Information Decoding

To evaluate the long-term functional capacity of the chronic window interface, we performed a neural decoding analysis classifying stimulus chromaticity (isoluminant RG vs. 100% contrast BW). The input features were constructed by concatenating gamma-band power (30–80 Hz) across all valid electrode channels and the entire stimulus presentation period, capturing the full spatiotemporal dynamics of the response. In Monkey J, decoding performance was high on Day 14 and remained robust at Day 35 (Fig. 8, left). While the accuracy gradually declined during the extended chronic phase, statistical analysis using a bootstrap test (1000 iterations) confirmed that decoding performance remained significantly above the chance level (50%) for all recording sessions ($p < 0.001$). This temporal modulation likely reflects the evolving physical and physiological state of the dural interface, such as the progressive dural thickening and signal attenuation discussed in previous sections. In Monkey K, decoding accuracy remained high, fluctuating from Day 7 through Day 28 (Fig. 8, right), with performance in all sessions significantly exceeding the chance level (bootstrap test, 1000 iterations, $p < 0.001$). Collectively, the longitudinal trajectory of the decoding performance quantitatively reflects the functional degradation of the electrode-tissue interface. While high classification accuracy was achieved during the initial month post-implantation, the subsequent progressive decline observed in Monkey J highlights the profound signal attenuation driven by chronic biological transitions, primarily tissue encapsulation. Rather than indicating robust long-term stability, these results demonstrate that the array retains statistically significant residual functionality over five months ($p < 0.001$). This considerable degradation underscores the fundamental limitations of the current biological interface, emphasizing that further advancements in material biocompatibility and dural seal design are required to mitigate progressive signal loss and sustain long-term functional performance.

4. Discussion

In this study, we developed a chronic cranial window interface integrated with a high-density µECoG array to achieve precise, visually guided monitoring of neural activity in the macaque visual cortex. A primary contribution of this work is the longitudinal evaluation and comparison of two distinct dural interface designs (a floating Tecoflex sheet versus a bonded silicone ring) to address the critical issue of maintaining chronic optical access. However, maintaining long-term optical clarity presented challenges. In Monkey J, direct visual access to the cortical surface was preserved for approximately two weeks before being obscured by tissue regrowth. In Monkey K, despite design modifications intended to mitigate tissue accumulation, visibility was compromised by post-surgical hemorrhage. Despite the eventual loss of optical transparency, the electrophysiological performance of the interface captured the dynamic biological transitions of the tissue environment. Longitudinal assessment demonstrated relatively stable impedance profiles in Monkey K during the post-acute period (Days 14–42) and statistically significant stimulus-induced gamma-band responses in Monkey J that persisted for over five months, albeit with progressive signal attenuation. While low-frequency VEPs were inherently attenuated by our recording configuration (local subdural reference combined with a common average reference), this setup prioritized the extraction of high-frequency gamma-band dynamics associated with local cortical activity. As an initial demonstration of feasibility, this transparent interface showed the ability to perform accurate co-registration of electrode sites with underlying vascular landmarks during the initial post-implantation period in one subject.

As shown in our initial demonstration, an important potential advantage of the transparent window interface is the ability to monitor the physical stability of the array in relation to cortical landmarks. In standard epidural implantations, longitudinal changes in functional maps are often confounded by the uncertainty of electrode positioning relative to the cortical surface [25]. While conventional methods rely on intraoperative photographs and terminal imaging, these static "snapshots" are insufficient to account for the ongoing volumetric changes of the brain caused by chronic physiological factors. The transparent window interface overcomes this limitation by enabling continuous, non-invasive longitudinal monitoring. In this study, visual inspection confirmed that the 64-channel µECoG array remained physically stable relative to the vascular landmarks, ruling out gross mechanical migration or detachment. However, quantitative image analysis revealed subtle micro-scale shifts of the array, measuring approximately 0.12 mm at one week and 0.20 mm at two weeks post-implantation (Fig. 3). While based on a single subject, these preliminary observations suggest that even when macroscopic stability is maintained, micro-scale physical shifts can occur. Given the fine functional organization of the cortex [26], such subtle displacements highlight the potential necessity of continuous spatial tracking in future high-resolution longitudinal studies to ensure accurate interpretation of spatiotemporal neural dynamics. Importantly, the session-to-session variability observed in our longitudinal data (Fig. 6) serves as a critical indicator of the ongoing micro-structural dynamics at the electrode-tissue interface. Furthermore, in the context of chronic recordings, these physical shifts continuously interact with state-dependent physiological modulations. Specifically, our recordings were conducted under

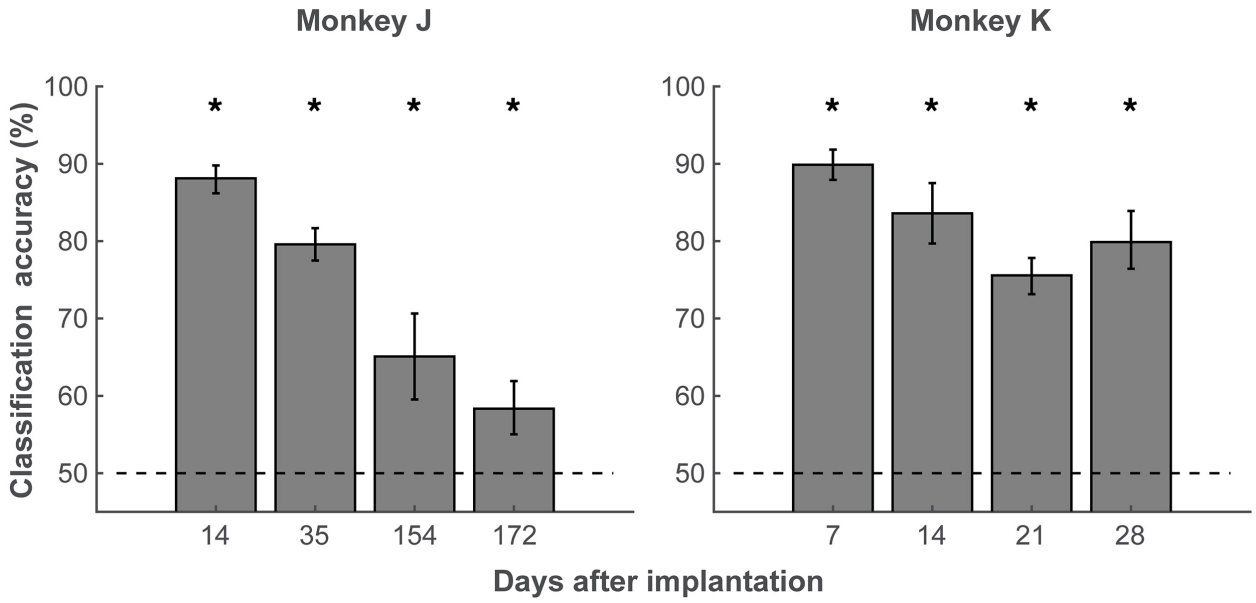

Fig. 8. Longitudinal performance of visual information decoding. Classification accuracy for discriminating between isoluminant red-green (RG) and 100% luminance-contrast black-white (BW) grating stimuli across recording sessions for Monkey J (left) and Monkey K (right). Decoding analysis was performed using a linear support vector machine (SVM) with a 10-fold cross-validation scheme, based on spatiotemporal gamma-band (30–80 Hz) power features aggregated across all valid channels and the entire stimulus duration. The total number of trials per session was 387, 383, 448, and 380 for Monkey J (Days 14, 35, 154, and 172) and 309, 310, 310, and 311 for Monkey K (Days 7, 14, 21, and 28), respectively. Error bars indicate 95% confidence intervals estimated via bootstrapping. The horizontal dashed line represents the chance level (50%). Asterisks (*) indicate statistical significance ($p < 0.001$, bootstrap test with 1000 iterations).

propofol anesthesia, which significantly attenuates visual-evoked gamma oscillations [27]. Under such pharmacologically suppressed conditions, the recorded spatial topographies likely become highly susceptible to distortion caused by even the subtle 0.20 mm physical shifts. Because these mechanical and physiological variables co-occur and continuously interact, it remains inherently challenging to definitively disentangle their respective contributions, resulting in the complex session-to-session variability observed. Beyond electrode localization, a fundamental advantage of the transparent window is the capability for continuous, non-invasive visual inspection of the cortical tissue. As demonstrated by our early detection of the subdural hematoma in Monkey K, this direct optical access is critical for assessing post-surgical complications and localized inflammation. Furthermore, it provides essential structural and biological context for interpreting the progressive degradation of electrophysiological signals—such as the observed attenuation in decoding accuracy—thereby eliminating the strict reliance on secondary neuroimaging or terminal histological endpoints to understand the evolving electrode-tissue interface.

Longitudinal impedance monitoring in Monkey K provided insight into the dynamic evolution of the electrode-tissue interface. Prior research indicates that implant impedance typically undergoes a biphasic evolution, shifting from an acute reactive phase characterized by a rapid initial rise (e.g., within the first 20 to 30 days) to a stable chronic plateau or gradual decline [25,28]. Our observations closely mirror this biphasic trend: impedance magnitudes increased markedly from their initial baseline by Day 7 (Fig. 4), consistent with the formation of a fibrous capsule [29], and subsequently transitioned into a steady plateau. To better contextualize our design within the broader field of chronic neural interfaces, Table 1 (Ref. [25,28,30,31,32]) summarizes comparable high-density μECoG and cranial window approaches in primate and rodent models, specifically focusing on *in vivo* longitudinal evaluations. In this study, we utilized a standard polyimide-based array with platinum (Pt) contacts, a material combination known for its stable electrical properties. While, as noted in the Methods, our quantitative impedance data were obtained from a single subject and therefore cannot be broadly generalized, it provides an illustrative initial demonstration. During the critical post-acute stabilization phase (Days 14–42 in our monitoring), the array maintained a stable median impedance of 59.7–74.6 kΩ. This compares favorably to the 120–300 kΩ ranges often reported in recent chronic custom arrays [25,30]. Furthermore, while a direct numerical comparison of absolute impedance is inappropriate due to substantial differences in electrode geometric surface area (i.e., 200 μm diameter in the present study versus

Table 1. Comparison of *in vivo* µECoG and cranial window interfaces in primates and rodents.

Study	Animal model	Substrate/Contact material	Cranial window	Channels (diameter/pitch)	Impedance (at 1 kHz)	Recording duration
Schendel et al., 2013 [25]	Rat	Parylene C/Pt	Glass window (epidural)	16 ch (200 µm/750 µm)	~150–300 kΩ	Up to 10 weeks
Woods et al., 2018 [28]	Rat	LCP or PI/Au	Epidural (no window)	61 ch (200 µm/400 µm)	~50–400 kΩ[1]	247–435 days
Chiang et al., 2020 [30]	Macaque	PI/Au	Sealed Ti chamber (no window)	294 ch (229 µm/610 µm)	~120–150 kΩ	~400 days
Griggs et al., 2021 [32]	Macaque	Transparent copolymer/Pt	Embedded artificial dura (MMAD)	32 ch (500 µm/2 mm)	~270 kΩ[1]	Acute
Donaldson et al., 2022 [31]	Mouse	PET/PEDOT:PSS	Polymer skull (epidural)	10 ch (~50 µm/1.2 mm[1])	~81.4 kΩ	>100 days
Present study	Macaque	PI/Pt	Glass window	64 ch (200 µm/1 mm)	59.7–74.6 kΩ[2]	172 days[3]

[1] Value estimated from the corresponding figure in the original publication.

[2] Median impedance range during the post-acute plateau period (Days 14–42) in Monkey K.

[3] Functional recordings were obtained through Day 172 in Monkey J and Day 28 in Monkey K. Impedance monitoring in Monkey K continued through Day 42 (6 weeks).

Abbreviations: PI, polyimide; LCP, liquid crystal polymer; PET, polyethylene terephthalate; PEDOT:PSS, poly(3,4-ethylenedioxythiophene) polystyrene sulfonate; MMAD, multi-modal artificial dura; Ti, titanium; Pt, platinum; Au, gold.

~50 µm in the cited study), this longitudinal stability generally parallels the chronic performance trends observed in recent advanced transparent arrays utilizing poly(3,4-ethylenedioxythiophene) polystyrene sulfonate (PEDOT:PSS) in mice [31]. Unlike traditional closed-chamber ECoG studies where tissue reactions are evaluated without direct optical access, our approach enabled direct, *in vivo* longitudinal observation of micro-hematoma dynamics and progressive window opacification, highlighting that optimizing the mechanical compliance of the dural seal is a key consideration for long-term multimodal interfaces alongside the electrode material itself.

While the conductivity of reactive tissue implies that the observed electrical stability does not entirely rule out gradual vertical displacement of the array from the cortex, classification accuracy remained robust during the initial month post-implantation (up to Day 35 in Monkey J and Day 28 in Monkey K; Fig. 8). However, a decline in performance was observed during the extended chronic phase (Days 154–172 in Monkey J). This reduction likely reflects progressive signal attenuation caused by the maturation and thickening of the connective tissue between the array and the cortical surface, which increases the physical distance between the electrodes and the signal sources. Even at these late time points, classification accuracy remained significantly above chance levels, indicating that the array retained some residual functionality. The focus on stimulus-induced gamma-band power as a primary metric was instrumental in maintaining this decoding performance, as this high-frequency component is less susceptible to the spatial averaging and signal cancellation inherent in our specific reference configuration compared to lower-frequency VEPs. This aligns with previous findings that µECoG arrays can yield information-rich signals despite the inevitable presence of encapsulation tissue [33]. However, rather than serving as a positive indicator of stable long-term performance, the considerable degradation in classification accuracy over the five-month period highlights the limitations of the current preparation. These findings underscore the critical need for further work to improve material biocompatibility to mitigate chronic signal attenuation.

While the window interface successfully supported chronic electrophysiological recording, maintaining long-term optical clarity remains a challenge, particularly regarding the prevention of hemorrhage. In Monkey K, the subdural hematoma/blood products remained visible beneath the chamber window up to Day 64. This complication may be attributed to the mechanical configuration of the dural interface. Unlike the "floating" Tecoflex sheet used in Monkey J, which accommodated brain pulsations through its structural flexibility, the silicone ring in Monkey K was rigidly fixed to the chamber and hermetically bonded to the glass window. This configuration likely created a biomechanical mismatch at the interface between the pulsating cortex and the stationary silicone ring. As highlighted in recent biomaterials research, even conventional flexible polymers can induce continuous tissue damage due to the modulus mismatch with ultra-soft brain tissue [34]. The hermetic bonding essentially constrained the silicone's ability to deform, concentrating continuous shear stress precisely at the junction with the cut dural edge. This localized mechanical stress could lead to recurrent micro-tearing of fragile neovessels within the regenerating tissue, a phenomenon previously noted in studies using silicone-based dural substitutes [35]. Indeed, previous reports have indicated that mechanical interactions between silicone-based artificial dura and the underlying cortex can cause tissue thinning and deformation [36]. Furthermore, placing the cortex under an impermeable glass window fundamentally alters local fluid dynamics. The absence of the native dura and the resulting restriction of normal cerebrospinal fluid flow may disrupt glymphatic clearance processes, which could further exacerbate the long-term fibrotic tissue response. The selection of materials also involves a trade-off between mechanical sealing capabilities and biomechanical compliance. Silicone elastomers are frequently employed in chronic window designs due to their ease of fabrication into complex geometries—such as the integrated ring used here—and their capacity to form robust hermetic bonds [35]. However, as evidenced by the persistent hemorrhage in our observation, these practical advantages are ultimately offset by the material's relative rigidity, which exacerbates interfacial trauma during continuous cortical displacement. These findings highlight a critical design constraint: while ensuring a hermetic seal against tissue invasion, the interface must possess profound mechanical compliance to mitigate localized stress and preserve the integrity of the underlying vasculature.

Based on these considerations, if we were to conduct future experiments, we would base our approach on Design 2. Although Design 1 provided better initial mechanical accommodation for brain pulsations, its inability to prevent peripheral tissue invasion ultimately led to a severe loss of optical access in our observation. Design 2, on the other hand, effectively mitigated this dural ingrowth during the observation period. To overcome its current limitation—interfacial trauma caused by the biomechanical mismatch and mechanical rigidity of the silicone—future iterations of Design 2 should refine the ring's architecture and material properties by utilizing thinner structures composed of highly compliant elastomers with lower elastic moduli, in line with recent advancements in neural interface materials [34]. By securely bonding such advanced compliant materials to the optical window, it is expected to create an optimal interface that maintains a physical barrier against tissue invasion while safely absorbing cortical displacement and minimizing localized stress on the vasculature.

Beyond the immediate benefit of visually guided implantation, the primary scientific value of this transparent

interface architecture lies in its potential for multimodal interrogation of neural circuits. By providing a platform that integrates high-density electrophysiology with optical access, this interface bridges the gap between macroscopic field potentials and microscopic cellular or hemodynamic activity. For instance, intrinsic signal optical imaging can be performed through the transparent areas of the window to map functional domains, such as color or orientation columns, with high spatial precision [6]. Correlating these hemodynamic maps with 64-channel µECoG signals offers a unique opportunity to dissect the neurovascular coupling mechanisms underlying functional architecture. Furthermore, the optical transparency of the interface is compatible with advanced imaging techniques like two-photon microscopy, enabling the simultaneous monitoring of single-cell calcium dynamics and local field potentials [17]. Finally, this platform is ideally suited for closed-loop optogenetic interventions. The transparent window allows for precise light delivery to target specific neural populations [37], while the µECoG array captures the resultant network-level oscillations and connectivity changes with millisecond precision, as demonstrated in non-human primates [36]. Thus, the developed window interface serves as a versatile platform for investigating the multiscale dynamics of primate cortical function.

We acknowledge several limitations in the present study. First, all neural recordings were acquired under anesthesia. Since anesthesia modulates the excitation-inhibition balance and can alter the spectral characteristics of visual-evoked gamma oscillations [27], the spatiotemporal response patterns observed here may not fully reflect the dynamics of the awake, behaving state. However, the demonstrated mechanical and electrical stability of the interface serves as a necessary foundation for transitioning to chronic experiments in awake primates. Second, regarding optical monitoring, this study focused primarily on structural co-registration using vascular landmarks. While the 64-channel interface is designed to support functional optical imaging, such as intrinsic signal or calcium imaging, a detailed cross-validation of these optical signals with high-density µECoG data was beyond the scope of this report and remains an important objective for follow-up research. Third, while we successfully demonstrated electrode tracking relative to vascular landmarks, this observation was limited to a single animal (Monkey J) due to post-surgical hemorrhage in the second subject. Therefore, this capability should currently be viewed as an initial demonstration of feasibility, providing a foundation for future studies to establish this methodology. Finally, the duration of functional data collection varied between subjects, with a shorter recording period for Monkey K due to the persistent hemorrhage complications. Nevertheless, the longitudinal impedance profiles in Monkey K suggested that the electrode-tissue interface remained functionally viable even when optical clarity was compromised, supporting the overall durability of the recording platform for long-term electrophysiological monitoring.

5. Conclusions

In conclusion, this study developed and evaluated a chronic cranial window interface that integrates 64-channel µECoG recording with optical access in the macaque visual cortex. By systematically comparing different dural interface strategies, our results highlight the critical mechanical and biological trade-offs required to mitigate fibrotic tissue invasion and hemorrhage. Although long-term maintenance of optical clarity remains a technical challenge—underscoring the requirement for mechanically compliant and hermetically sealed interface designs—the system supports longitudinal high-density recording, revealing the dynamic fluctuations in functional channel yield that reflect the evolving physical and physiological environment of the tissue interface. Additionally, as an initial demonstration, the transparent interface enabled direct visual validation of electrode positions during the early post-surgical phase. By elucidating the design requirements for simultaneous electrical recording and initial optical monitoring, this study provides foundational insights for the future development of multimodal platforms. Ultimately, advancing such integrated approaches will be essential for dissecting neural circuit dynamics and bridging the gap between local cellular activity and global network states in the primate brain.

Availability of Data and Materials

The raw data supporting the conclusions of this article will be made available by the authors, without undue reservation.

Author Contributions

XW: Methodology, Software, Validation, Formal analysis, Investigation, Data curation, Writing—review & editing, Writing—original draft, Visualization. XZ: Investigation, Writing—review & editing. CL, DH: Investigation, Writing—review & editing. HT: Conceptualization, Methodology, Software, Validation, Formal analysis, Investigation, Resources, Data curation, Writing—review & editing, Writing—original draft, Visualization, Supervision, Project administration, Funding acquisition. All authors read and approved the final manuscript. All authors have participated sufficiently in the work and agreed to be accountable for all aspects of the work.

Ethics Approval and Consent to Participate

All experimental procedures involving non-human primates were approved by the Animal Care and Use Committee of Zhejiang University (Permit Number: ZJU20240745) and were conducted in accordance with the relevant guidelines and regulations of Zhejiang University for the care and use of laboratory animals.

Acknowledgment

Not applicable.

Funding

This work was supported by grants from the Shenzhen Medical Research Fund (B2504002) and the National Natural Science Foundation of China (31872776) to HT.

Conflicts of Interest

The authors declare no conflicts of interest.

Declaration of AI and AI-Assisted Technologies in the Writing Process

During the preparation of this manuscript, the authors used Gemini (Google) to assist with English language polishing, text structuring, drafting specific sections, and writing custom scripts for data analysis. After using this tool, the authors rigorously reviewed, tested, and edited both the text and the generated code, taking full responsibility for the accuracy of the data analysis and the final content of the publication. No AI tools were used in the collection of data or the direct production of images.

Supplementary Material

Supplementary material associated with this article can be found in the online version at https://doi.org/10.31083/JIN52601.

References

[1] Buzsáki G, Anastassiou CA, Koch C. The origin of extracellular fields and currents—EEG, ECoG, LFP and spikes. Nature Reviews Neuroscience. 2012; 13: 407–420. https://doi.org/10.1038/nrn3241

[2] Asano E, Juhász C, Shah A, Muzik O, Chugani DC, Shah J, et al. Origin and propagation of epileptic spasms delineated on electrocorticography. Epilepsia. 2005; 46: 1086–1097. https://doi.org/10.1111/j.1528-1167.2005.05205.x

[3] Chao ZC, Nagasaka Y, Fujii N. Long-term asynchronous decoding of arm motion using electrocorticographic signals in monkeys. Frontiers in Neuroengineering. 2010; 3: 3. https://doi.org/10.3389/fneng.2010.00003

[4] Khodagholy D, Gelinas JN, Thesen T, Doyle W, Devinsky O, Malliaras GG, et al. NeuroGrid: recording action potentials from the surface of the brain. Nature Neuroscience. 2015; 18: 310–315. https://doi.org/10.1038/nn.3905

[5] Viventi J, Kim DH, Vigeland L, Frechette ES, Blanco JA, Kim YS, et al. Flexible, foldable, actively multiplexed, high-density electrode array for mapping brain activity in vivo. Nature Neuroscience. 2011; 14: 1599–1605. https://doi.org/10.1038/nn.2973

[6] Tanigawa H, Lu HD, Roe AW. Functional organization for color and orientation in macaque V4. Nature Neuroscience. 2010; 13: 1542–1548. https://doi.org/10.1038/nn.2676

[7] Kaiju T, Inoue M, Hirata M, Suzuki T. High-density mapping of primate digit representations with a 1152-channel μECoG array. Journal of Neural Engineering. 2021; 18: 036025. https://doi.org/10.1088/1741-2552/abe245

[8] Moses DA, Leonard MK, Makin JG, Chang EF. Real-time decoding of question-and-answer speech dialogue using human cortical activity. Nature Communications. 2019; 10: 3096. https://doi.org/10.1038/s41467-019-10994-4

[9] Schalk G, Leuthardt EC. Brain-computer interfaces using electrocorticographic signals. IEEE Reviews in Biomedical Engineering. 2011; 4: 140–154. https://doi.org/10.1109/RBME.2011.2172408

[10] Fukushima M, Saunders RC, Mullarkey M, Doyle AM, Mishkin M, Fujii N. An electrocorticographic electrode array for simultaneous recording from medial, lateral, and intrasulcal surface of the cortex in macaque monkeys. Journal of Neuroscience Methods. 2014; 233: 155–165. https://doi.org/10.1016/j.jneumeth.2014.06.022

[11] Hermes D, Miller KJ, Noordmans HJ, Vansteensel MJ, Ramsey NF. Automated electrocorticographic electrode localization on individually rendered brain surfaces. Journal of Neuroscience Methods. 2010; 185: 293–298. https://doi.org/10.1016/j.jneumeth.2009.10.005

[12] Nabavi A, Black PM, Gering DT, Westin CF, Mehta V, Pergolizzi RS, Jr, et al. Serial intraoperative magnetic resonance imaging of brain shift. Neurosurgery. 2001; 48: 787–798. https://doi.org/10.1097/00006123-200104000-00019

[13] Brang D, Dai Z, Zheng W, Towle VL. Registering imaged ECoG electrodes to human cortex: A geometry-based technique. Journal of Neuroscience Methods. 2016; 273: 64–73. https://doi.org/10.1016/j.jneumeth.2016.08.007

[14] Dykstra AR, Chan AM, Quinn BT, Zepeda R, Keller CJ, Cormier J, et al. Individualized localization and cortical surface-based registration of intracranial electrodes. NeuroImage. 2012; 59: 3563–3570. https://doi.org/10.1016/j.neuroimage.2011.11.046

[15] Blasdel GG, Salama G. Voltage-sensitive dyes reveal a modular organization in monkey striate cortex. Nature. 1986; 321: 579–585. https://doi.org/10.1038/321579a0

[16] Ts'o DY, Frostig RD, Lieke EE, Grinvald A. Functional organization of primate visual cortex revealed by high resolution optical imaging. Science. 1990; 249: 417–420. https://doi.org/10.1126/science.2165630

[17] Ohki K, Chung S, Ch'ng YH, Kara P, Reid RC. Functional imaging with cellular resolution reveals precise micro-architecture in visual cortex. Nature. 2005; 433: 597–603. https://doi.org/10.1038/nature03274

[18] Percie du Sert N, Hurst V, Ahluwalia A, Alam S, Avey MT, Baker M, et al. The ARRIVE guidelines 2.0: Updated guidelines for reporting animal research. PLoS Biology. 2020; 18: e3000410. https://doi.org/10.1371/journal.pbio.3000410

[19] Oostenveld R, Fries P, Maris E, Schoffelen JM. FieldTrip: Open source software for advanced analysis of MEG, EEG, and invasive electrophysiological data. Computational Intelligence and Neuroscience. 2011; 2011: 156869. https://doi.org/10.1155/2011/156869

[20] Tanigawa H, Majima K, Takei R, Kawasaki K, Sawahata H, Nakahara K, et al. Decoding distributed oscillatory signals driven by memory and perception in the prefrontal cortex. Cell Reports. 2022; 39: 110676. https://doi.org/10.1016/j.celrep.2022.110676

[21] Zhou T, Kawasaki K, Suzuki T, Hasegawa I, Roe AW, Tanigawa H. Mapping information flow between the inferotemporal and prefrontal cortices via neural oscillations in memory retrieval and maintenance. Cell Reports. 2023; 42: 113169. https://doi.org/10.1016/j.celrep.2023.113169

[22] Fan RE, Chang KW, Hsieh CJ, Wang XR, Lin CJ. LIBLINEAR: A library for large linear classification. Journal of Machine Learning Research. 2008; 9: 1871–1874.

[23] Miller KJ, Leuthardt EC, Schalk G, Rao RPN, Anderson NR, Moran DW, et al. Spectral changes in cortical surface potentials during motor movement. The Journal of Neuroscience. 2007;

27: 2424–2432. https://doi.org/10.1523/JNEUROSCI.3886-06.2007
[24] Ray S, Maunsell JHR. Different origins of gamma rhythm and high-gamma activity in macaque visual cortex. PLoS Biology. 2011; 9: e1000610. https://doi.org/10.1371/journal.pbio.1000610
[25] Schendel AA, Thongpang S, Brodnick SK, Richner TJ, Lindevig BDB, Krugner-Higby L, et al. A cranial window imaging method for monitoring vascular growth around chronically implanted micro-ECoG devices. Journal of Neuroscience Methods. 2013; 218: 121–130. https://doi.org/10.1016/j.jneumeth.2013.06.001
[26] Hubel DH, Wiesel TN. Ferrier lecture. Functional architecture of macaque monkey visual cortex. Proceedings of the Royal Society of London. Series B, Biological Sciences. 1977; 198: 1–59. https://doi.org/10.1098/rspb.1977.0085
[27] Aggarwal A, Brennan C, Shortal B, Contreras D, Kelz MB, Proekt A. Coherence of Visual-Evoked Gamma Oscillations Is Disrupted by Propofol but Preserved Under Equipotent Doses of Isoflurane. Frontiers in Systems Neuroscience. 2019; 13: 19. https://doi.org/10.3389/fnsys.2019.00019
[28] Woods V, Trumpis M, Bent B, Palopoli-Trojani K, Chiang CH, Wang C, et al. Long-term recording reliability of liquid crystal polymer μECoG arrays. Journal of Neural Engineering. 2018; 15: 066024. https://doi.org/10.1088/1741-2552/aae39d
[29] Williams JC, Hippensteel JA, Dilgen J, Shain W, Kipke DR. Complex impedance spectroscopy for monitoring tissue responses to inserted neural implants. Journal of Neural Engineering. 2007; 4: 410–423. https://doi.org/10.1088/1741-2560/4/4/007
[30] Chiang CH, Lee J, Wang C, Williams AJ, Lucas TH, Cohen YE, et al. A modular high-density μECoG system on macaque vlPFC for auditory cognitive decoding. Journal of Neural Engineering. 2020; 17: 046008. https://doi.org/10.1088/1741-2552/ab9986
[31] Donaldson PD, Navabi ZS, Carter RE, Fausner SML, Ghanbari L, Ebner TJ, et al. Polymer Skulls With Integrated Transparent Electrode Arrays for Cortex-Wide Opto-Electrophysiological Recordings. Advanced Healthcare Materials. 2022; 11: e2200626. https://doi.org/10.1002/adhm.202200626
[32] Griggs DJ, Khateeb K, Zhou J, Liu T, Wang R, Yazdan-Shahmorad A. Multi-modal artificial dura for simultaneous large-scale optical access and large-scale electrophysiology in non-human primate cortex. Journal of Neural Engineering. 2021; 18: 055006. https://doi.org/10.1088/1741-2552/abf28d
[33] Nurse ES, John SE, Freestone DR, Oxley TJ, Ung H, Berkovic SF, et al. Consistency of Long-Term Subdural Electrocorticography in Humans. IEEE Transactions on Biomedical Engineering. 2018; 65: 344–352. https://doi.org/10.1109/TBME.2017.2768442
[34] Xie Y, Peng Y, Guo J, Liu M, Zhang B, Yin L, et al. Materials and devices for high-density, high-throughput micro-electrocorticography arrays. Fundamental Research. 2025; 5: 17–28. https://doi.org/10.1016/j.fmre.2024.01.016
[35] Arieli A, Grinvald A, Slovin H. Dural substitute for long-term imaging of cortical activity in behaving monkeys and its clinical implications. Journal of Neuroscience Methods. 2002; 114: 119–133. https://doi.org/10.1016/s0165-0270(01)00507-6
[36] Yazdan-Shahmorad A, Diaz-Botia C, Hanson TL, Kharazia V, Ledochowitsch P, Maharbiz MM, et al. A Large-Scale Interface for Optogenetic Stimulation and Recording in Nonhuman Primates. Neuron. 2016; 89: 927–939. https://doi.org/10.1016/j.neuron.2016.01.013
[37] Nassi JJ, Avery MC, Cetin AH, Roe AW, Reynolds JH. Optogenetic Activation of Normalization in Alert Macaque Visual Cortex. Neuron. 2015; 86: 1504–1517. https://doi.org/10.1016/j.neuron.2015.05.040